geosciences

MDPI

Article

Efficient 3D Inversion of the Marine Electrical-Source Time Domain Electromagnetic Method Based on the Footprint Technique

Xianxiang Wang *, Shanmei Li, Zefan Hu and Qing Sun

National Key Laboratory of Uranium Resources Exploration-Mining and Nuclear Remote Sensing, East China University of Technology, Nanchang 330013, China; lishanmei0919@163.com (S.L.); hzf9396@163.com (Z.H.); sqstrive@163.com (Q.S.)

* Correspondence: wangxianxiang09@163.com

Highlights

What are the main findings?

- This study establishes a highly efficient 3D inversion framework for the Marine Electrical-Source TDEM method, grounded in the moving footprint technique. Unlike conventional approaches that compute global sensitivity, this method dynamically identifies the specific electromagnetic sensitivity region (the footprint domain) for each transmitter–receiver pair and constructs the sensitivity matrix exclusively within these localized, high-sensitivity zones.
- Through comprehensive numerical simulations, we elucidated the governing mechanisms by which offset, time delay, seawater thickness, and resistivity modulate the spatial extent of the footprint domain. These findings provide critical insights into the spatiotemporal diffusion characteristics of TDEM fields within shallow marine environments, offering a theoretical basis for optimizing survey parameters.

What are the implications of the main findings?

- The most significant implication is that large-scale 3D surveys are now computationally feasible. Previously, the massive data volume from moving transmitter–receiver systems made 3D inversion prohibitively slow or memory-intensive. By drastically reducing computational costs and memory requirements, this method allows geophysicists to process vast datasets that were previously impractical.

Abstract

Marine electric-source time domain electromagnetic (TDEM) surveys typically involve the simultaneous movement of transmitters and receivers, which generates a large number of transmitter–receiver pairs. This acquisition geometry creates notable challenges for 3D inversion, mainly because of the large data volume and high computational cost. However, the electromagnetic "sensitive region" for each transmitter–receiver pair is much smaller than the full survey area. Based on this feature, we propose an efficient 3D inversion approach using the footprint technique. By clearly defining the sensitivity region, referred to as the footprint domain, for each pair, the method builds the sensitivity matrix only within localized subsurface regions that significantly affect the observed response. This approach greatly reduces both forward modeling cost and memory requirements. The forward modeling adopts an integral equation method combined with cosine transforms for fast 3D field computation, while the inversion framework uses a regularized conjugate-gradient algorithm, further accelerated by parallel computing under footprint domain constraints.

Check for updates

Received: 28 February 2026
Revised: 22 March 2026
Accepted: 25 March 2026
Published: 1 April 2026

Copyright: © 2026 by the authors. Licensee MDPI, Basel, Switzerland. This article is an open access article distributed under the terms and conditions of the Creative Commons Attribution (CC BY) license.

Numerical simulations also examine the effects of offset, time channel, seawater thickness, and resistivity on the footprint domain, helping clarify the spatiotemporal diffusion behavior of TDEM fields in shallow marine environments. Tests on representative models show that the proposed method remains stable and accurate under complex geological conditions while significantly improving computational efficiency. In particular, the footprint domain technique improves inversion speed by about 55% compared with full domain inversion. These results indicate that the proposed approach provides a reliable and scalable option for large-scale 3D inversion of marine TDEM data.

Keywords: time domain electromagnetic method; electrical source; efficient 3D inversion; footprint technique

1. Introduction

In recent years, the marine controlled-source electromagnetic (MCSEM) method has played a crucial role in the exploration of hydrocarbon and mineral resources [1–3]. Owing to the high conductivity of seawater, time domain electromagnetic (EM) signals attenuate rapidly in deep water environments; consequently, frequency domain marine EM methods are predominantly employed for deep-sea surveys. Airwaves significantly contaminate marine EM signals, and their influence increases in both magnitude and spatial extent as water depth decreases [4]. When water depth is less than 300 m, airwaves dominate the frequency domain EM response, posing substantial challenges for data interpretation [5]. Due to differences in propagation velocity and arrival time, TDEM can effectively separate airwave signals from subsurface EM responses, providing a distinct advantage for shallow water exploration [6–10].

TDEM systems can be categorized into loop-source and electric-source configurations based on the transmitter type. In loop-source TDEM, a closed loop acts as the transmitter. However, the electromagnetic field generated by a loop source attenuates rapidly within the subsurface, resulting in limited penetration depth and reduced sensitivity to resistive targets [11–16]. In contrast, electric-source TDEM employs a long grounded wire as the transmitter, significantly increasing the depth of investigation relative to loop-source systems and providing high detection accuracy for both conductive and resistive targets [17]. For the *Ex* component excited by an electric source, exploration depth and resolution are strongly dependent on the transmitter–receiver offset: small offsets are more sensitive to shallow targets, whereas larger offsets enhance coupling with deeper geological structures [18,19].

Marine electric-source TDEM surveys are characterized by an acquisition configuration in which both the transmitter and receiver move simultaneously, typically generating large datasets with thousands of transmitter–receiver pairs. To interpret such data, early studies mainly focused on 1D and 2D inversion strategies. For 1D inversion, Lippert et al. successfully applied Occam and Marquardt algorithms, respectively, to marine time domain EM data [20], while Moghadas et al. systematically evaluated the impact of different inversion strategies on 1D results [21]. However, the validity of 1D assumptions is often limited by complex geology. Cai et al. showed that steep seafloor topography with dips greater than 30° can cause clear distortions in 1D inversion results [22]. To handle these structural complexities, 2D inversion has proven to be more reliable. Frafjord et al. used the MARE2DEM code and showed that 2D inversion can recover subsurface electrical structures even when induced polarization effects are present [23]. Similarly, Li et al. combined MARE2DEM with cosine transforms for multichannel TDEM data and confirmed that 2D

models provide better geological consistency than 1D models [24]. Despite the success of these lower-dimensional methods, they still cannot fully represent the three-dimensional complexity of marine settings. Some attempts at full 3D inversion have been reported. For example, Holten et al. applied a conjugate-gradient scheme for 3D anisotropic inversion of marine TDEM data [25]. However, due to the high computational cost, their work was limited to relatively small models. Although recent algorithmic developments have improved forward modeling and inversion efficiency in other geophysical fields [26–29], the large volume of spatial data in marine TDEM remains a major challenge. As a result, even with advances in computing hardware and 3D methods, inversion speed is still a key limitation, which restricts the practical use of large-scale 3D inversion in towed electric-source TDEM surveys.

Because airborne electromagnetic (AEM) systems are compact and exhibit highly localized sensitivity, only the model cells within the footprint domain—namely, those that contribute significantly to the receiver response—need to be considered in modeling and inversion. This strategy drastically reduces the number of grid cells involved and substantially improves computational efficiency. Cox and Zhdanov were the first to introduce the footprint concept into 3D inversion of frequency domain AEM data, proposing a moving footprint-based inversion strategy that reduced both memory usage and computational complexity by several orders of magnitude, thereby greatly accelerating computation and improving storage efficiency [30]. Cox et al. subsequently extended this approach to 3D inversion of time domain AEM data [31]. Gribenko et al. further applied the footprint technique to large-scale 3D magnetotelluric (MT) inversion, achieving similarly notable improvements in efficiency [32]. Liu et al. proposed a footprint-guided modeling method for AEM, in which the entire survey area is partitioned into multiple subdomains based on the footprint's spatial distribution, enabling efficient forward simulation within each subdomain [33]. Qi et al. implemented 3D inversion of time domain AEM data on unstructured meshes using the footprint technique and investigated the influence of topography on inversion results [34]. Zhang et al. extracted local meshes from a global mesh based on footprint distribution patterns. They achieved 3D AEM inversion on unstructured grids by projecting the Jacobian matrix computed on local meshes back onto the global mesh [35]. In summary, the footprint technique has greatly improved the efficiency of 3D AEM inversion and has made large-scale 3D inversion more feasible.

Despite these advances, the moving footprint technique has mainly been used for compact survey systems, and its application is still largely limited to AEM methods. Only a few studies have extended it to ground-based or marine electromagnetic 3D inversion. However, towed electric-source TDEM surveys share several key features with AEM systems. Both involve simultaneous motion of the transmitter and receiver, and their depth of investigation is mainly controlled by the transmitter–receiver offset. At small offsets, the spatial range of electromagnetic sensitivity in electric-source TDEM is also highly localized, which is similar to AEM systems. Therefore, the moving footprint approach developed for AEM can be adapted for 3D inversion of towed marine electric-source TDEM data.

To deal with the computational challenges in 3D inversion of marine electric-source TDEM data, this study introduces the moving footprint technique into the inversion framework. By systematically analyzing the effects of offset, time, seawater properties, and receiver position on the spatial extent of the footprint domain in shallow marine environments, we develop a footprint-weighted sensitivity-matrix construction method. This approach substantially reduces both the computational scale and the storage requirements of the time domain sensitivity matrix, thereby significantly alleviating the inversion computational burden. Representative marine numerical models are constructed, and comparative 3D inversions are performed using both full domain and footprint-restricted approaches.

Numerical experiments demonstrate that the footprint-based inversion achieves accuracy comparable to that of full domain inversion while offering markedly improved computational efficiency, thereby confirming the effectiveness and practicality of the footprint technique for 3D inversion of marine electric-source TDEM data.

2. 3D Modeling and Inversion

2.1. 3D Modeling Theory Based on the Integral Equation Method

This paper employs a three-dimensional integral equation (IE) method for forward numerical modeling. In this framework, the total electromagnetic fields $\boldsymbol{E}$, $\boldsymbol{H}$ are decomposed into the sum of the background fields $\boldsymbol{E}_b$, $\boldsymbol{H}_b$, and the anomalous fields $\boldsymbol{E}_a$, $\boldsymbol{H}_a$:

$$\begin{aligned} \boldsymbol{E} &= \boldsymbol{E}_b + \boldsymbol{E}_a \\ \boldsymbol{H} &= \boldsymbol{H}_b + \boldsymbol{H}_a \end{aligned} \tag{1}$$

The anomalous fields $\boldsymbol{E}_a$, $\boldsymbol{H}_a$ are the scattered electromagnetic fields generated by residual currents arising from the presence of anomalous conductivity $\Delta\sigma$. Within the anomalous body, the anomalous fields can be expressed as volume integrals of the residual current over the anomalous region:

$$\begin{aligned} \boldsymbol{E}_a(\boldsymbol{r}_j) &= \iiint \boldsymbol{G}_b^E(\boldsymbol{r}_j|\boldsymbol{r}) \cdot j(\boldsymbol{r}) dv = \boldsymbol{G}^E(j) \\ \boldsymbol{H}_a(\boldsymbol{r}_j) &= \iiint \boldsymbol{G}_b^H(\boldsymbol{r}_j|\boldsymbol{r}) \cdot j(\boldsymbol{r}) dv = \boldsymbol{G}^H(j) \end{aligned} \tag{2}$$

Here, $j(\mathrm{r})$ denotes the residual current density within the anomalous region; $\boldsymbol{G}_b^E$, and $\boldsymbol{G}_b^H$ are the background electric and magnetic Green's tensors, respectively. The vector $\boldsymbol{r}$ represents the integration point within the anomalous body, and $\boldsymbol{r}_j$ is the observation point, which may lie either inside or outside the anomalous region.

The TDEM fields are related to the frequency domain electromagnetic (FDEM) fields through the following expression:

$$f(t) = \frac{1}{2\pi} \int_{-\infty}^{+\infty} F(\omega) \cdot G(\omega) e^{i\omega t} d\omega \tag{3}$$

In this expression, $f(t)$ represents the TDEM field, $F(\omega)$ denotes the FDEM field, t is time, ω is the angular frequency, and $G(\omega)$ is the Fourier spectrum of the source. The sine–cosine integrals involve Bessel functions; in this study, a 201-point digital Hankel filter is employed [36].

2.2. 3D Inversion Algorithm Based on Regularized Conjugate Gradient Method

To address the ill-posed nature of the inverse problem, a Tikhonov parametric functional is introduced to ensure the stability of the inversion:

$$P^{\alpha}(m) = F(m) + \alpha s(m) \rightarrow \min \tag{4}$$

Here, α is the regularization parameter, $s(m)$ is the stabilizing functional, and $F(m)$ is the data misfit functional, defined as:

$$F(m) = (A(\mathrm{m}) - d)^T C_d^{-1} (A(\mathrm{m}) - d) \tag{5}$$

In Equation (5), d represents the observed data, $A(\mathrm{m})$ is the forward response corresponding to model parameters m, and C_d is a weighting matrix designed to balance the contributions of data acquired at different times and offsets during the inversion process.

A minimum-gradient-support (MGS) functional in the vertical direction is employed to enhance sensitivity to vertical structural variations, leading to sharper vertical boundaries in the inversion results. This property is particularly advantageous for resolving the thickness of horizontally layered or thin reservoir targets [37]:

$$s_{\mathrm{MVS}}(\Delta\sigma) = \iiint_{\mathrm{V}} \left[\frac{(\Delta\sigma)^2}{\iint_S (\Delta\sigma)^2 dxdy + \beta^2} \right] dz \tag{6}$$

where β is a focusing parameter, and S denotes the horizontal cross-section of the rectangular domain V.

Sensitivity Matrix Calculation

The sensitivity matrix describes the linearized relationship between perturbations in model parameters and the resulting variations in the observed data and plays a central role in inversion efficiency. Within the integral equation framework, the sensitivity can be computed as the inner product of the additional field generated by a unit electric or magnetic dipole source located at the receiver position $\boldsymbol{r}_j$ and the primary field:

$$\begin{aligned} s_E(\boldsymbol{r}') &= \sqrt{\int_\Omega \iint_\Sigma \left(\boldsymbol{G}^E(\boldsymbol{r}_j \mid \boldsymbol{r}') \cdot \boldsymbol{E}(\boldsymbol{r}')\right)^2 ds d\omega} \\ s_H(\boldsymbol{r}') &= \sqrt{\int_\Omega \iint_\Sigma \left(\boldsymbol{G}^H(\boldsymbol{r}_j \mid \boldsymbol{r}') \cdot \boldsymbol{H}(\boldsymbol{r}')\right)^2 ds d\omega} \end{aligned} \tag{7}$$

Here, $s_E(\boldsymbol{r}')$, $s_H(\boldsymbol{r}')$ denote the sensitivities of the electric and magnetic fields, respectively, with respect to conductivity variations. This formulation avoids explicit construction and storage of the full Jacobian matrix; instead, only the Green's functions and electric field vectors are retained, thereby reducing memory requirements and improving computational efficiency.

3. Analysis of Factors Affecting the Footprint in Marine Electric-Source TDEM Surveys

In marine electric-source TDEM surveys, a single survey area often involves hundreds of transmitter–receiver pairs. A full inversion requires calculating the sensitivity for each pair over the entire inversion domain, which leads to an extremely large sensitivity matrix and brings heavy storage and computational demands. As a result, if the size of the sensitivity matrix is not reduced, inversion efficiency remains very low, even when parallel multi-core computing is used.

Similar to AEM systems, the marine electric-source TDEM method is also a typical acquisition configuration in which the transmitter and receiver move simultaneously. Its depth of investigation is strongly influenced by the transmitter–receiver offset. When the offset is small, the investigation depth is limited; as the offset increases, the exploration depth correspondingly increases. In AEM methods, footprint techniques are widely used because the transmitter and receiver coils are usually mounted on the same aircraft. In such cases, each data point is sensitive only to a limited region around it. In contrast, marine TDEM uses electric sources and array receivers to measure the Ex field, resulting in a more complex sensitivity distribution. Several factors, including offset, time, seawater thickness, seawater resistivity, and subsurface resistivity, influence the spatial pattern of the footprint.

To illustrate this behavior, a model with an offset of 2000 m, a seawater depth of 300 m, a seawater resistivity of 0.3 Ω·m, and a subsurface half-space resistivity of 1 Ω·m is considered. The sensitivity distribution at a seabed receiver location at a time of 100 s is calculated, as shown in Figure 1. The results indicate that the core sensitivity region is concentrated near the line connecting the transmitter and receiver, with higher sensitivity values oc-

curring closer to both the transmitter and the receiver. However, this region occupies only a relatively small portion of the entire inversion volume. By restricting computations to subsurface regions that contribute significantly to the observed response—namely, the footprint domain—the storage requirements of the sensitivity matrix can be greatly reduced, computational memory consumption can be minimized, and inversion time can be shortened. This provides important feasibility support for large-scale 3D inversion.

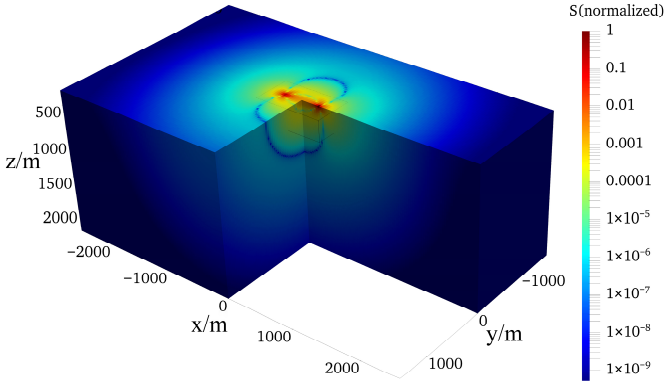


Figure 1. Marine TDEM sensitivity distribution at an offset of 500 m, a subsurface resistivity of 1 Ω·m, and a time of 100 s.

In the following sections, the influences of these factors on the footprint characteristics of marine electric-source TDEM are systematically analyzed.

3.1. Influence of Time

To investigate the influence of time on the footprint domain, a representative model is constructed with a seawater depth of 300 m, a seawater resistivity of 0.3 Ω·m, and a seabed half-space resistivity of 1 Ω·m. Both the transmitter and the receiver are positioned on the seafloor, with a fixed offset of 2000 m. To ensure consistent characterization of sensitivity distributions at different times, the sensitivity at each time step is first normalized by its corresponding maximum value. Subsequently, the normalized sensitivity is cumulatively integrated over the 3D model domain. Lower thresholds can improve efficiency but may miss important sensitivity, while higher thresholds bring only small gains in accuracy and greatly increase the computation area. Therefore, the footprint domain is defined as the region that accounts for more than 90% of the total contribution. This choice keeps a good balance between accuracy and efficiency and is consistent with previous studies [38,39]. Figure 2 shows the spatial evolution of the footprint domain at four representative times: 0.1 s, 1 s, 10 s, and 100 s. The normalized sensitivity thresholds corresponding to the footprint boundaries at each time are extracted, and the side lengths of the footprint domain in the inline, crossline, and depth directions are statistically summarized in Table 1.

Analysis of Figure 2 and Table 1 indicates that the spatial extent of the footprint domain exhibits a non-uniform expansion with increasing time. This behavior reflects the outward diffusion of TDEM field sensitivity over time, accompanied by a gradual increase in the effective investigation region. Specifically, at times of 0.1 s, 1 s, 10 s, and 100 s, the footprint extents in the inline direction are 3120 m, 3300 m, 3720 m, and 3720 m, respectively; in the crossline direction, they are 1260 m, 1500 m, 2200 m, and 2200 m, respectively; and in the depth direction, they are 540 m, 620 m, 860 m, and 860 m, respectively. These results demonstrate that the footprint domain is largest in the inline direction and smallest in the depth direction. Moreover, as time increases, lateral expansion in the inline and crossline directions is relatively limited. In contrast, vertical expansion in the depth direction is more pronounced, indicating a strong time dependence of the effective investigation depth.

Notably, once the time exceeds approximately 10 s, the footprint domain stabilizes in all three directions and no longer expands significantly. This suggests that the effective detection depth of the TDEM field reaches a quasi-steady state beyond this time, and further extending the observation window contributes little to increasing spatial coverage.

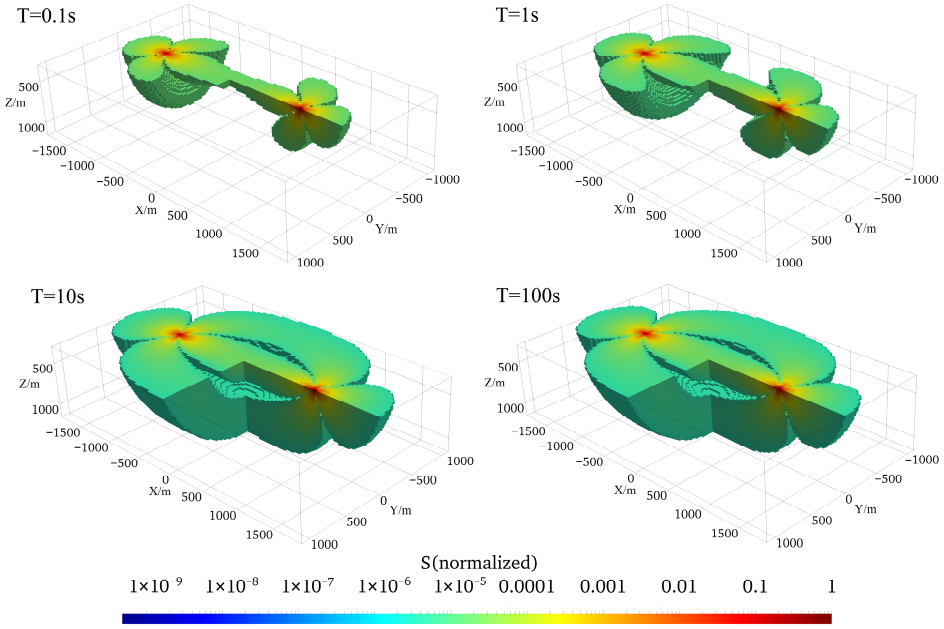


Figure 2. Temporal evolution of the footprint domain for an offset of 2000 m, seawater depth of 300 m, seawater resistivity of 0.3 Ω·m, subsurface resistivity of 1 Ω·m, with both transmitter and receiver located on the seafloor.

Table 1. Statistical extents of the footprint domain at different times under identical model conditions: offset = 2000 m, seawater depth = 300 m, seawater resistivity = 0.3 Ω·m, subsurface resistivity = 1 Ω·m, with transmitter and receiver positioned on the seafloor. S (normalized) means that the sensitivity at each time step is normalized by its maximum value.

Time (s)	S (Normalized)	Inline (m)	Crossline (m)	Depth (m)
0.1	0.000013065	3120	1260	540
1	0.0000083624	3300	1500	620
10	0.0000036035	3720	2220	860
100	0.0000034798	3720	2220	860

3.2. Influence of Seawater

In marine electric-source TDEM surveys, a commonly used acquisition configuration involves seabed-towed deployment, in which both the transmitter and the receiver are positioned directly on or near the seafloor. Conventional inversion practices typically focus on the subsurface beneath the seafloor and treat the overlying seawater as a known background medium that is excluded from the inversion. However, under this simplifying assumption, the extent to which the electrical properties and thickness of the seawater layer influence the spatial characteristics of the footprint domain has not been systematically evaluated. To address this issue, this section examines the impact of seawater on the footprint domain.

3.2.1. Including the Sensitivity Distribution in Seawater

In marine electromagnetic inversion, the overlying seawater is generally regarded as a known background medium and is therefore neglected. Accordingly, two alternative strategies can be adopted when defining the footprint domain: one that includes the

contribution of sensitivity distributed within the seawater layer, and another that neglects the sensitivity contribution from seawater. To assess the impact of these two approaches on the spatial extent of the footprint domain, a comparative analysis is performed.

When the sensitivity distribution within seawater is included, the temporal evolution of the footprint domain is shown in Figure 3. In this case, the footprint domain exhibits a temporal evolution pattern similar to that described in Section 2.1, characterized by gradual expansion followed by stabilization. A quantitative comparison indicates that, when the sensitivity contribution from seawater is considered, the footprint domain dimensions in the inline, crossline, and depth directions are 3480 m, 1920 m, and 800 m, respectively. These values are smaller than those obtained when the seawater contribution is neglected (3720 m, 2220 m, and 860 m, respectively). This difference arises because seawater, acting as a conductive layer, absorbs and attenuates a portion of the electromagnetic energy, thereby reducing the electromagnetic field's sensitivity to deeper subsurface structures. When the seawater sensitivity contribution is ignored, the resulting footprint domain is correspondingly larger. For this reason, and to enhance inversion accuracy, the scheme that neglects the seawater sensitivity contribution is adopted in all subsequent analyses.

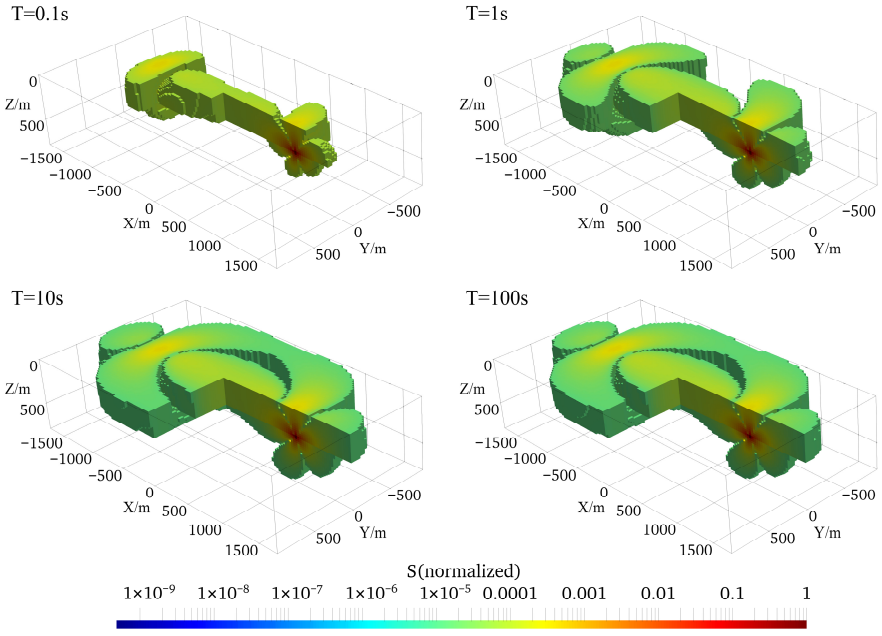


Figure 3. Temporal evolution of the Footprint domain when sensitivity within seawater is included, with the transmitter and receiver located on the seafloor.

3.2.2. Influence of Seawater Depth

To investigate the influence of seawater depth on the footprint domain, a series of numerical simulations is conducted for seawater depths ranging from 100 m to 700 m.

Based on the footprint domain extents at the late-time stable stage (T = 100 s) across different seawater depths, as shown in Figure 4 and Table 2, seawater depth is found to influence the footprint domain scale to some extent. To further quantify this relationship, the variations in footprint extent along the inline, crossline, and depth directions are fitted as functions of seawater depth.

The fitting results (Figure 5) show that, in the inline direction, the footprint extent decreases monotonically with increasing seawater depth and stabilizes at approximately 400–500 m. In the crossline direction, the footprint extent gradually decreases from 2400 m at a seawater depth of 100 m to 1740 m at 700 m, entering a stable state within the 600–700 m depth range. This trend is characterized by a rapid decrease at shallow depths followed by

a slower decline at greater depths. In the depth direction, the footprint extent decreases with increasing seawater depth and stabilizes at approximately 300–400 m.

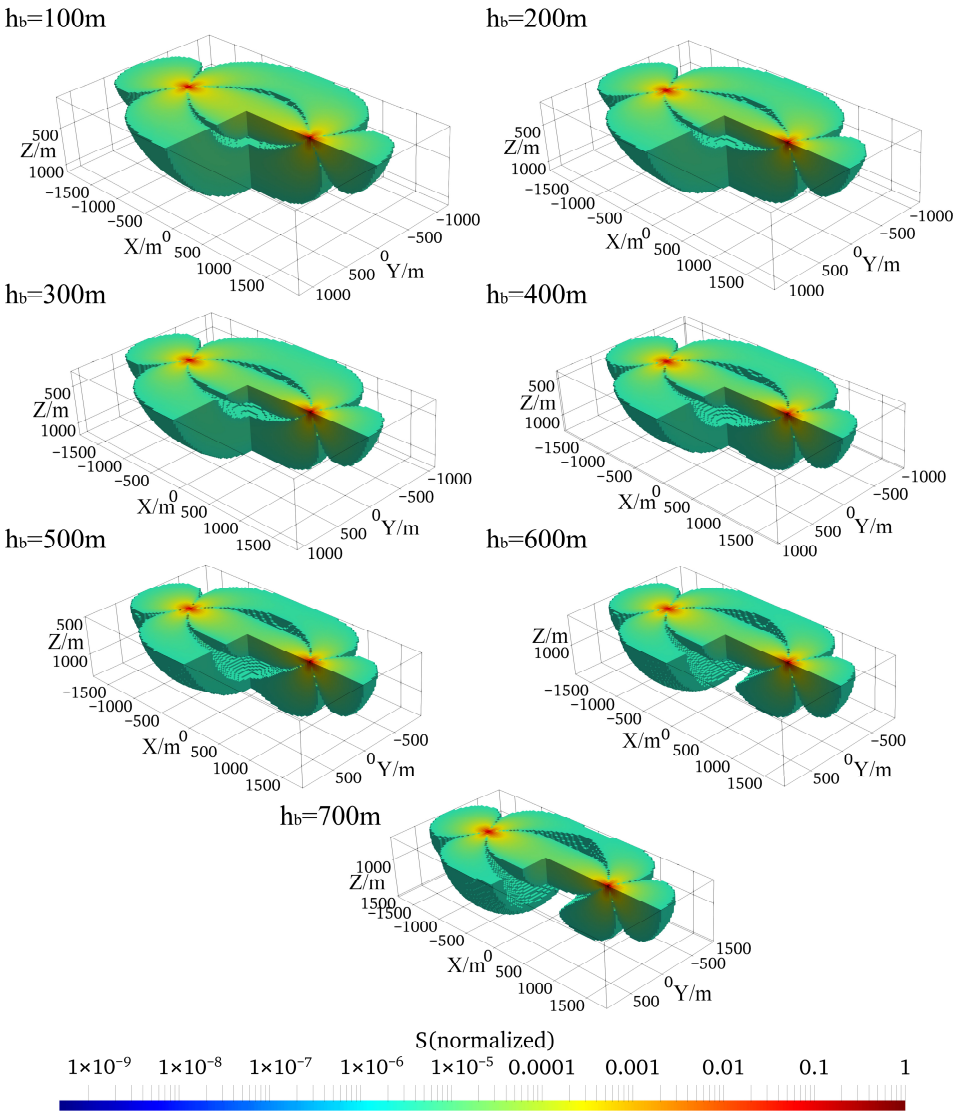


Figure 4. Variation in the footprint domain with seawater depth ranging from 100 m to 700 m at a fixed time of T = 100 s.

Table 2. Statistics of footprint domain extents (corresponding to regions contributing more than 90% of the total sensitivity) at t = 100 s for seawater depths ranging from 100 m to 700 m.

Ocean Depth (m)	S (Normalized)	Inline (m)	Crossline (m)	Depth (m)
100	0.0000041046	3960	2400	1000
200	0.0000035724	3840	2340	920
300	0.0000034798	3720	2220	860
400	0.0000033403	3660	2040	820
500	0.0000032775	3600	1920	820
600	0.000003202	3600	1800	820
700	0.0000031569	3600	1740	820

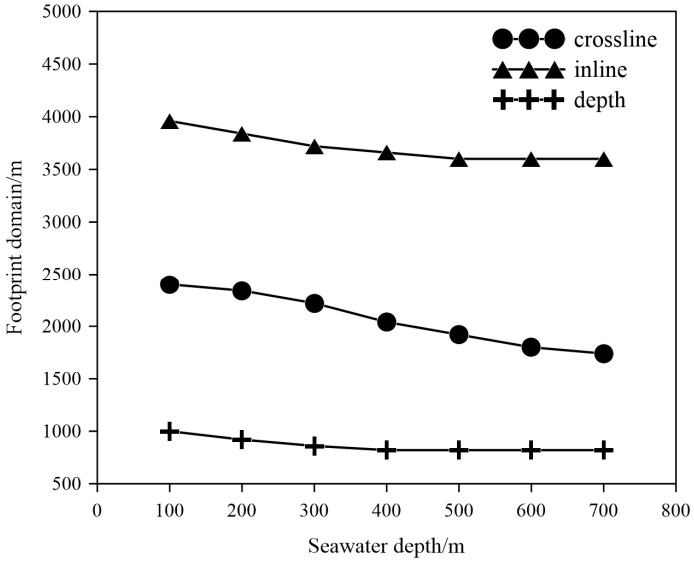


Figure 5. Relationship between seawater depth and footprint domain extent in the inline, crossline, and depth directions.

3.3. Influence of Resistivity

To investigate the influence of subsurface resistivity on the footprint domain, this section presents a comparative analysis of footprint domain variations under different resistivity conditions.

By comparing the footprint domain results for subsurface resistivities of 1 Ω·m (Figure 2, Table 1) and 0.5 Ω·m (Figure 6), it is observed that subsurface resistivity has a measurable influence on the footprint domain. During the early transient stage (T = 0.1 s), when the subsurface resistivity is 0.5 Ω·m, the footprint domain extents in the inline, crossline, and depth directions are 2880 m, 1260 m, and 520 m, respectively. When the resistivity increases to 1 Ω·m, these extents increase to 3120 m, 1320 m, and 540 m, respectively, indicating that the footprint domain expands with increasing subsurface resistivity during the early stage.

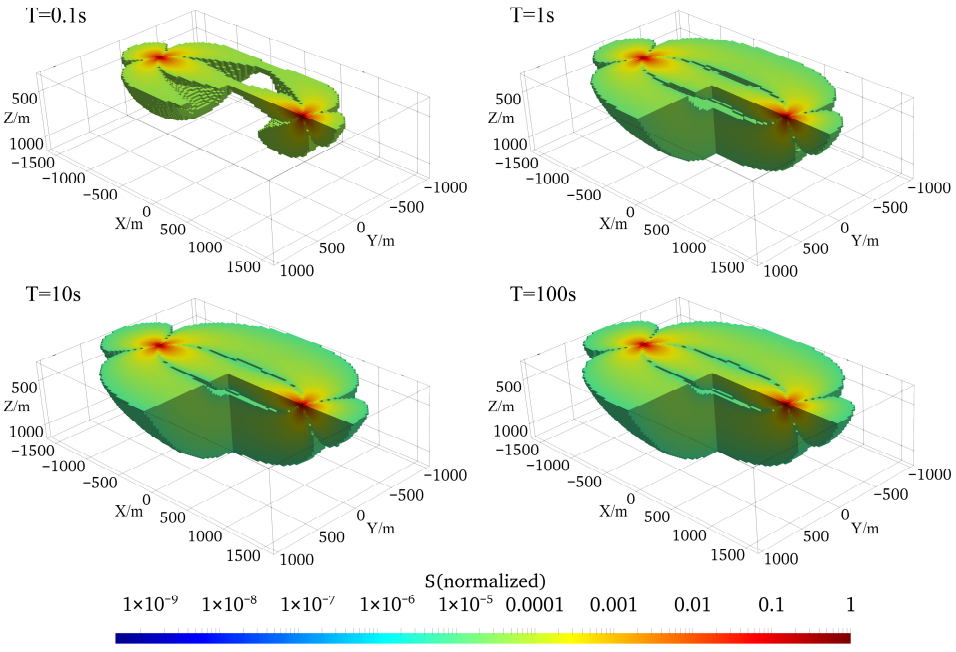


Figure 6. Variation in the footprint domain for a subsurface resistivity of 0.5 Ω·m.

At the late-time stable stage (T = 100 s), increasing the subsurface resistivity from 0.5 Ω·m to 1 Ω·m causes the footprint extent in the inline direction to increase from 3300 m to 3720 m and in the crossline direction from 2100 m to 2220 m, while the depth extent remains unchanged at 860 m. This indicates that, during the late stage, higher resistivity continues to expand the footprint domain in the horizontal directions, whereas its influence on the vertical detection depth is negligible.

In summary, increasing subsurface resistivity not only enlarges the footprint domain during the early transient stage but also continues to extend its horizontal (inline and crossline) coverage after stabilization at late times, while exerting little influence on the vertical (depth) extent of the footprint domain.

3.4. Influence of Transmitter and Receiver Location

3.4.1. Influence of Offsets

The exploration depth in marine TDEM surveys is significantly influenced by the transmitter–receiver offset. When the offset is small, the detection range is highly limited; however, the exploration depth increases substantially as the offset increases. This section investigates the influence of offset on the footprint domain. The footprint variations for offsets of 500 m, 1000 m, and 2000 m are shown in Figures 7, 8 and 2, respectively. By comparing the sensitivity diffusion characteristics across different offsets, it is observed that the footprint domain expands as the offset increases, with a more pronounced expansion in the horizontal directions than in the vertical. This indicates that electromagnetic field sensitivity is concentrated primarily in the horizontal plane and attenuates rapidly with depth. Furthermore, an analysis of offsets at different times shows that the footprint domain stabilizes earlier for smaller offsets, whereas larger offsets require a longer time to stabilize (Tables 3 and 4). This demonstrates that, as the transmitter–receiver offset increases, the electromagnetic field propagates over greater distances, thereby requiring more time to stabilize.

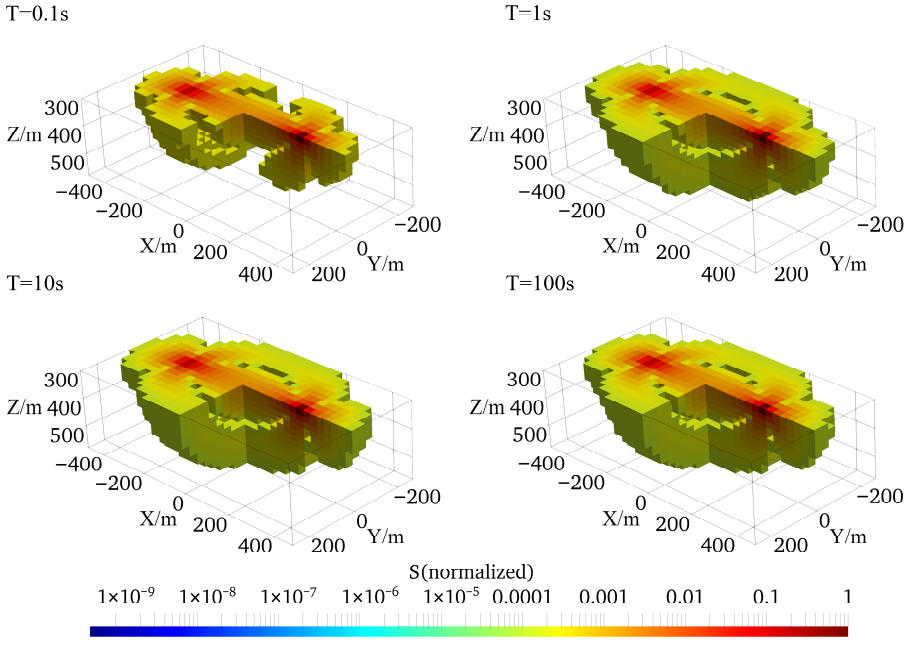


Figure 7. Variation in the footprint domain at an offset of 500 m.

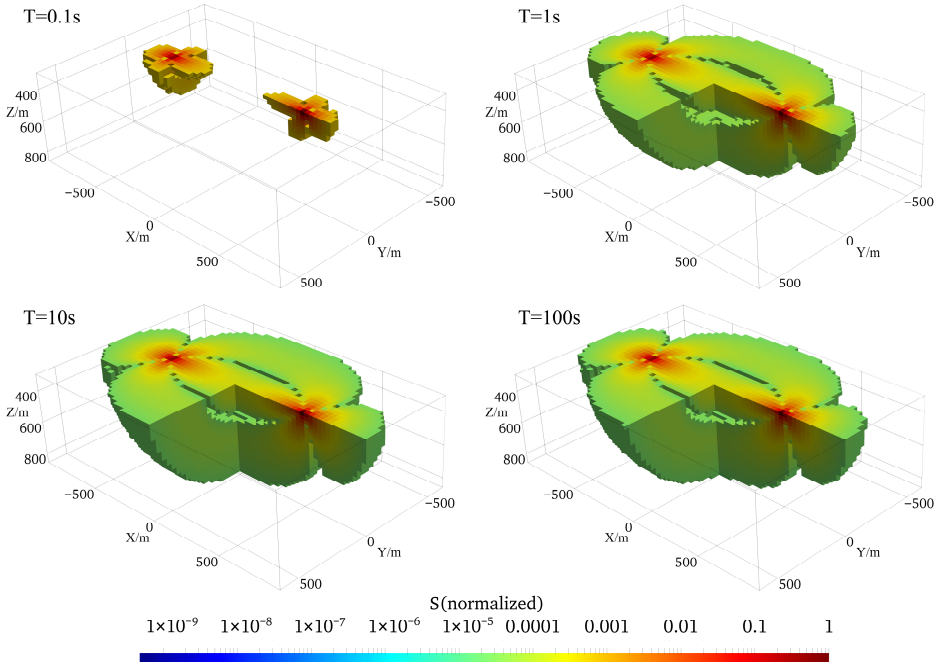


Figure 8. Variation in the footprint domain encompassing more than 90% of the sensitivity at an offset of 1000 m.

Table 3. Statistics of footprint domain side lengths at an offset of 500 m.

Time (s)	S (Normalized)	Inline (m)	Crossline (m)	Depth (m)
0.1	0.00023163	900	420	220
1	0.00012356	960	540	260
10	0.00011169	960	540	280
100	0.00011105	960	540	280

Table 4. Statistics of side lengths of the footprint domain containing more than 90% of the sensitivity at an offset of 1000 m.

Time (s)	S (Normalized)	Inline (m)	Crossline (m)	Depth (m)
0.1	0.00048368	1380	360	180
1	0.000033714	1800	1080	480
10	0.000021986	1860	1200	540
100	0.000021582	1860	1260	560

Because the late-time footprint domain is larger than the early-time footprint domain, it is generally used as a representative approximation of the complex, time-dependent footprint domain. Through numerical fitting, the relationships between the footprint domain dimensions and the offset are derived, as shown in Figure 9: inline = $1.86L + 6.063298 \times 10^{-13}$, crossline = $1.1142857L - 30$, depth = $0.39714286L + 70$. The footprint domain expands approximately linearly with increasing offset, with horizontal expansion being significantly greater than vertical expansion. This further confirms that the electromagnetic response is primarily concentrated near the horizontal surface and that the sensitivity of marine TDEM measurements decays rapidly with depth.

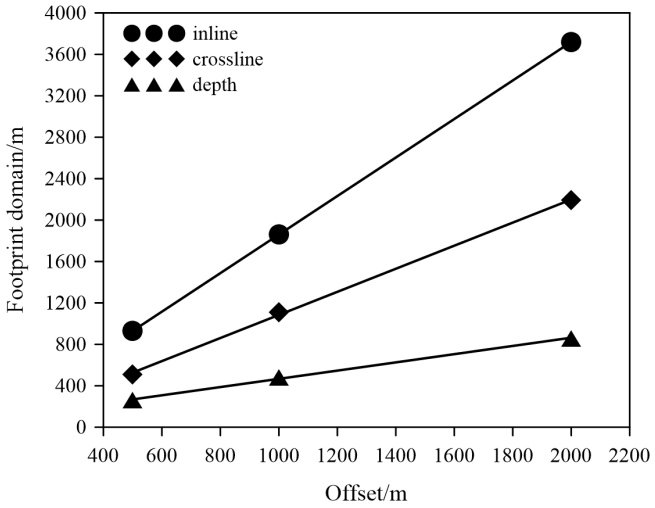


Figure 9. Relationship between the offset r and footprint axis widths.

3.4.2. Transmitter and Receiver Located at the Sea Surface

Marine TDEM detection systems typically employ a seafloor-towed configuration for deploying the transmitter and receiver. To assess the impact of relocating the transmitter and receiver to a sea-surface floating configuration on the footprint domain, we calculate the footprint domain's distribution characteristics at different observation times under sea-surface detection conditions.

Figure 10 illustrates the temporal evolution of the footprint domain for detection points located at the sea surface when the sensitivity contribution from seawater is excluded. In contrast, Figure 11 shows the corresponding results when the seawater sensitivity contribution is included. A comparison of Figures 10 and 11 indicates that both computational approaches follow the typical temporal evolution of electromagnetic responses, with the footprint domain tending to stabilize at late times.

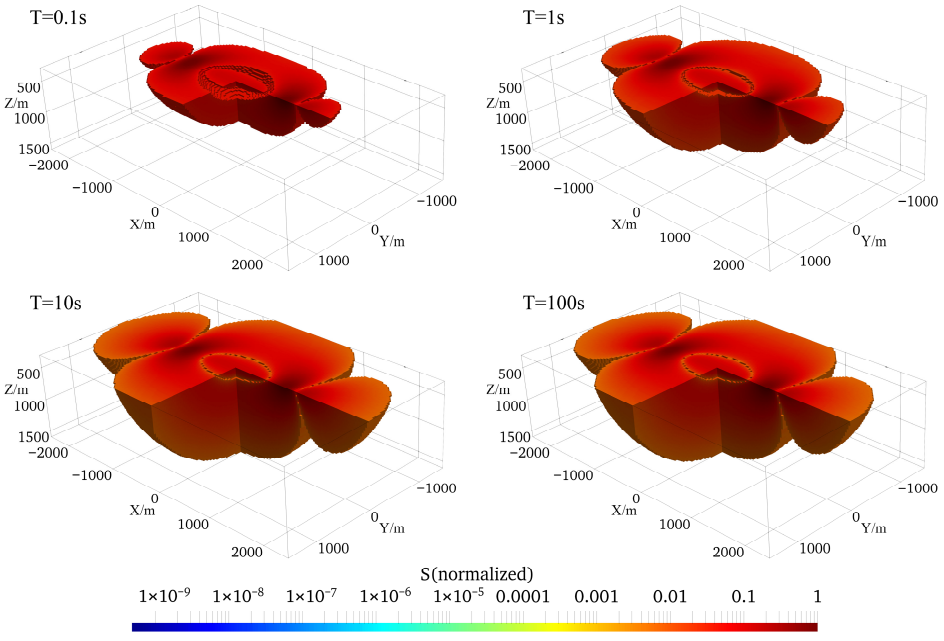


Figure 10. Temporal evolution of the footprint domain when the survey point is at the sea surface and seawater is excluded from the model.

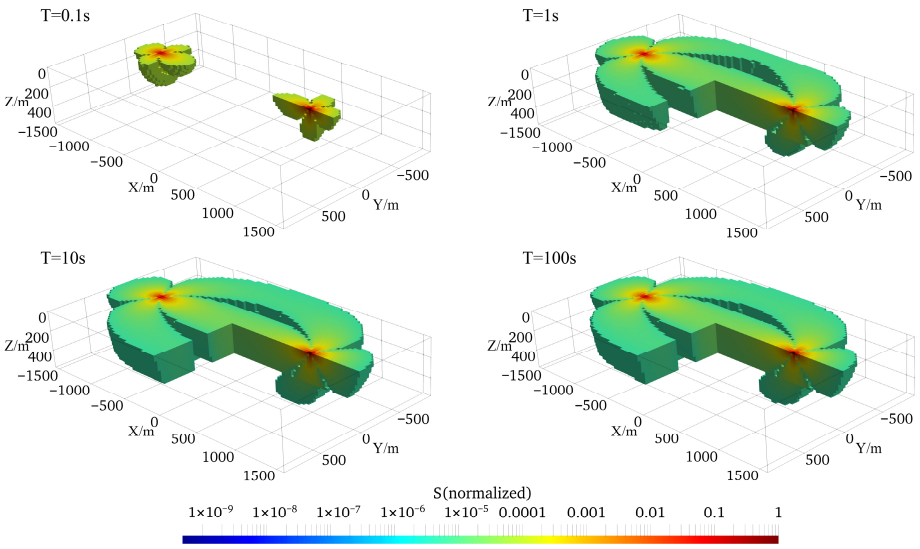


Figure 11. Temporal evolution of the footprint domain when the survey point is at the sea surface and seawater is included in the model.

When the detection point is located at the sea surface, the late-time footprint domain dimensions excluding seawater contributions (inline/crossline/depth = 4860 m/3000 m/1300 m) are significantly larger than those obtained when seawater contributions are included (3150 m/1860 m/580 m). This discrepancy arises from the strong absorption and attenuation of electromagnetic waves by seawater, which acts as a conductive medium. Consequently, if the influence of seawater is neglected in sea-surface deployments, the footprint domain becomes excessively diffused throughout the spatial domain. In contrast, when the seawater contribution is taken into account, the sensitive zone becomes highly concentrated beneath the detection point, substantially reducing the effective detection range. This phenomenon highlights the decisive influence of detection point placement on the spatial distribution of the footprint domain: seafloor deployment can effectively suppress seawater effects, thereby enabling more precise focusing on deep subsurface formations.

3.5. Summary and Analysis of Footprint Influencing Factors

Based on the comparative analyses presented in this chapter, the factors influencing the calculation of the footprint domain range in shallow-water marine TDEM surveys can be summarized as follows.

Time Factor: The footprint domain expands gradually over time, reflecting the outward diffusion of electromagnetic-field sensitivity. As time increases further, the footprint domain progressively stabilizes. Because a complex nonlinear relationship governs the temporal evolution of the footprint domain, the late-time footprint domain can be used as a representative approximation of the time-dependent footprint domain. This substitution also improves inversion accuracy.

Seawater Factor: When the spatial contribution of seawater is neglected, the calculated footprint domain range is larger than that obtained when seawater is included. Moreover, a considerable portion of the footprint domain may lie within the seawater layer, which is not the primary target of investigation. Seawater resistivity also exerts a significant influence: as resistivity decreases, the footprint domain expands in the inline and crossline directions but contracts in the depth direction. Similarly, seawater depth affects the footprint domain, with the inline, crossline, and depth dimensions all decreasing as seawater depth increases, until stabilization occurs beyond a certain depth. These results indicate that seawater properties have a pronounced impact on the range of the footprint domain.

Subsurface Resistivity Factor: As subsurface resistivity increases, the early-time footprint domain decreases in all directions (inline, crossline, and depth). After numerical stabilization at late times, resistivity primarily influences the inline direction, where higher resistivity corresponds to a reduced footprint range. In contrast, no significant effects are observed in the crossline or depth directions during the late stage.

Acquisition System Configuration Factors: (1) Offset: A linear relationship exists between the footprint domain dimensions and the transmitter–receiver offset L: inline = 1.86L + 6.063298 × 10^{-13}, crossline = 1.1142857L − 30, depth = 0.39714286L + 70. Increasing the offset expands the footprint domain in all directions, indicating a strong dependence of the footprint range on the offset. (2) Detection Point Location: When the detection point is located at the sea surface and seawater is excluded from the inversion, the footprint domain becomes excessively large. Conversely, when seawater is included, a substantial portion of the footprint domain is confined to the seawater layer, with only a limited extent extending into the target subsurface region. Comparison of these two scenarios demonstrates that detection point placement has a decisive influence on both the size and spatial distribution of the footprint domain.

In summary, the footprint domain is not a fixed geometric region but a dynamic sensitive space jointly controlled by time, seawater depth, subsurface resistivity, and acquisition system configuration. For 3D marine TDEM inversion, the footprint domain should therefore be dynamically defined according to the actual marine environment and observation parameters. This strategy avoids static or oversimplified assumptions and enables a balanced optimization of computational efficiency and imaging accuracy.

4. Synthetic Models

To verify the reliability and computational efficiency of 3D inversion for marine electric-source TDEM data based on footprint technology, two complex synthetic models were constructed for inversion testing.

4.1. Hydrocarbon Reservoir Model

To validate the detection capability of the electric-source TDEM method for resistive targets (such as hydrocarbon reservoirs) and to assess the reliability of inversion results based on footprint technology, a 3D marine hydrocarbon reservoir model was established according to the typical geometric and electrical characteristics of shallow-sea reservoirs. The model is configured with a seawater depth of 300 m and a seawater resistivity of 0.3 Ω·m. The spatial extent of the anomalous body is defined as 1835 < x < 6125 m, 3160 < y < 5160 m, and 550 < z < 2450 m. The cell dimensions in the x-, y-, and z-directions are 130 m, 80 m, and 100 m, respectively. As shown in Figure 12, the background resistivity is 1 Ω·m.

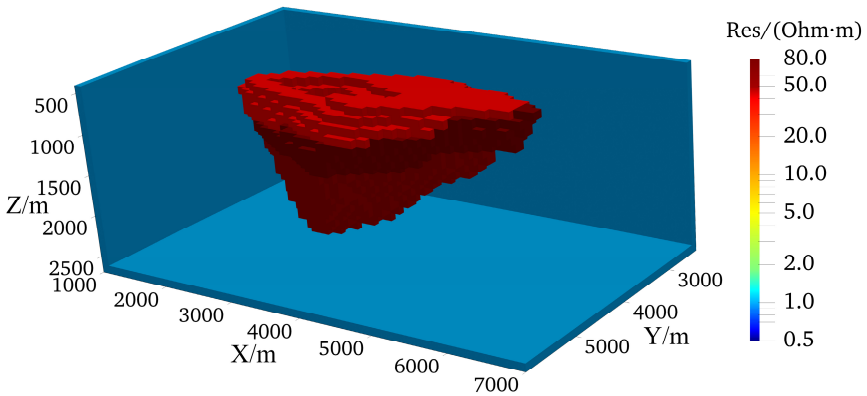


Figure 12. True model and model discretization for the hydrocarbon reservoir model.

The hydrocarbon reservoir region adopts a three-layer vertical resistivity structure: the upper layer has a resistivity of 40 Ω·m, the middle layer 80 Ω·m, and the lower layer 50 Ω·m. The resistive layer with a resistivity of 80 Ω·m is used to simulate the main hydrocarbon-bearing reservoir. In comparison, the overlying and underlying layers (40 Ω·m and 50 Ω·m) represent the overburden and the sub-reservoir or surrounding rocks, respectively. This configuration more realistically reflects the typical electrical stratification characteristics of hydrocarbon reservoirs in shallow marine environments.

The survey lines and observation points are deployed as follows. A total of eight survey lines are arranged and uniformly distributed along the y-direction at positions Y = [3000:300:5400] m. On each survey line, transmitters are deployed at 600 m intervals within the range X = [−2500:600:10100] m, while receivers are placed at 300 m intervals within the range X = [800:300:6800] m, as illustrated in Figure 13. Considering that high-frequency signals are susceptible to environmental interference and skin effects, the frequency range is set to $10^{(-5:0.15:4)}$ Hz and subsequently transformed into the time domain using a cosine transform. Due to the relatively low resistivity of both the background medium and anomalous bodies in marine environments, as well as the reduced stability of early-time signals affected by skin effects and propagation velocity, a later time window is selected for analysis compared with that used in land-based TDEM surveys. As shown by the temporal evolution of the footprint in Section 3, the exploration capability in the marine environment is very limited at 0.1 s. In contrast, the exploration depth stabilizes after about 100 s. Based on this, the time window is chosen accordingly. Therefore, the time window is set to $10^{(-0.7:0.1:3.3)}$ s.

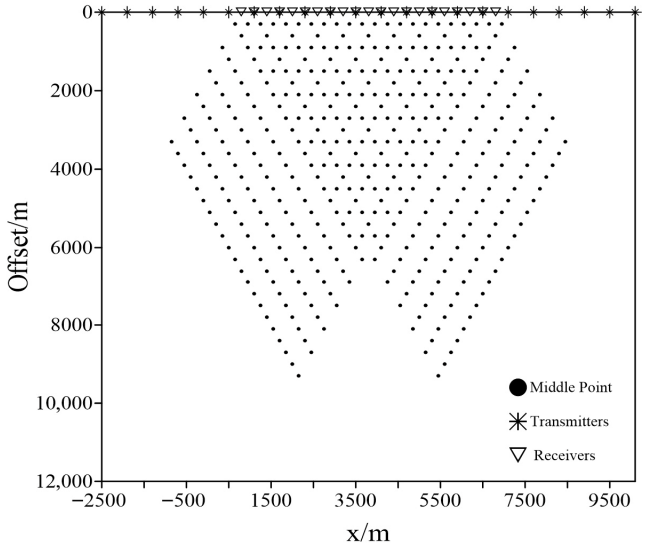


Figure 13. Survey configuration for hydrocarbon reservoir model.

The inversion region is defined as X = 800 ∼ 7100 m and Y = 2050 ∼ 6500 m. A 3D non-uniform mesh is generated within this region, with a total grid count of 20 × 13 × 13 in the x-, y-, and z-directions, respectively. In the x–y plane, grid density is dynamically adjusted according to the distribution of the anomalous body: denser grids, with a minimum grid size of 250 m, are used in regions containing the anomaly, while sparser grids, with a maximum grid size of 400 m, are applied in regions without anomalies or with gradually varying electrical properties. In the vertical direction, finer discretization is employed near the surface to enhance resolution, with a minimum grid size of 50 m, and the grid size gradually increases with depth, reaching a maximum of 300 m to balance computational efficiency and deep imaging requirements.

This section evaluates the effectiveness of the footprint technique in 3D inversion using the established marine hydrocarbon reservoir model. To ensure a fair comparison, both full domain sensitivity inversion and footprint-based inversion were conducted under identical conditions, including the same initial model, regularization parameters, and number of iterations (60). Figure 14 presents the spatial distribution of inversion resistivity values greater than 5 Ω·m after the 60th iteration for both schemes, providing an intuitive comparison of their imaging capabilities for high-resistivity anomalies corresponding to hydrocarbon reservoirs.

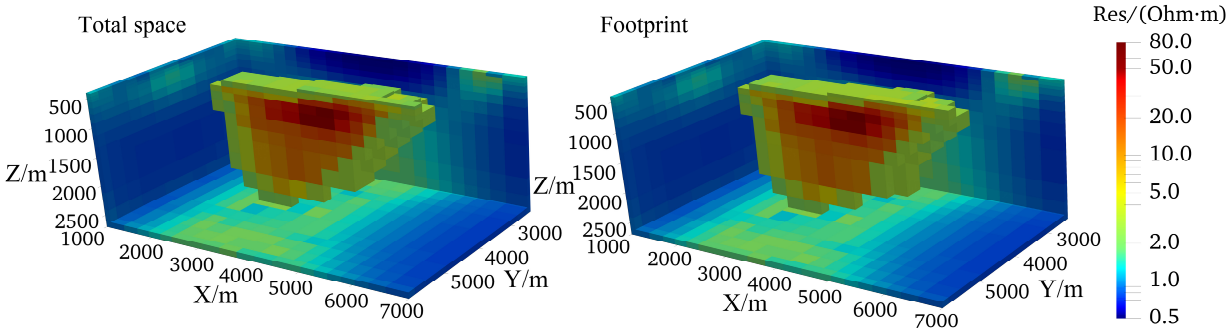


Figure 14. Comparison of inversion results between the footprint-domain and full domain approaches (**Left**): full domain inversion result; (**Right**): footprint-domain inversion result.

Comparison of the morphology and resistivity distribution of the 3D inversion results shows that the footprint-domain-based results closely match those obtained from conventional full domain inversion, thereby validating the reliability of the proposed method. In terms of computational efficiency, the footprint-domain technique demonstrates significant advantages. The conventional full domain inversion required approximately 420 min per iteration, whereas the footprint-domain inversion required only 250 min, corresponding to an overall computational efficiency improvement of approximately 55%. Memory consumption was also substantially reduced. This improvement mainly results from the intelligent selection of the footprint domain based on offset, with more pronounced efficiency gains for measurement points with smaller offsets. These results indicate that incorporating the footprint-domain technique into marine TDEM inversion significantly enhances computational performance while maintaining inversion accuracy.

As the number of inversion iterations increased to 60, the rate of misfit reduction gradually slowed (Figure 15), indicating relatively fast convergence of the algorithm. The slice results of the 3D inversion (Figure 16) reveal several key features. First, the marine TDEM method provides good delineation of the boundaries of the high-resistivity body, particularly demonstrating high vertical resolution for the upper interface. Second, for deeper and smaller-scale anomalous bodies, the inversion does not fully recover the high-resistivity characteristics. Third, resistivity recovery in shallow regions is significantly better than that in deeper regions. These effects are primarily attributed to the weak intensity of secondary field signals generated by deep high-resistivity bodies, which undergo strong attenuation during propagation through seawater and surrounding rocks, making them difficult to resolve.

To further validate the reliability of the inversion results, measurement points with offsets of 1200 m, 3000 m, 4800 m, 6600 m, and 8400 m along the survey line Y = 4800 m were selected. The forward responses of the inversion model were compared with the original observed data. As shown in Figure 17, the modeled curves from the inversion results agree well with the observed data across all offsets, confirming the reliability of the inversion.

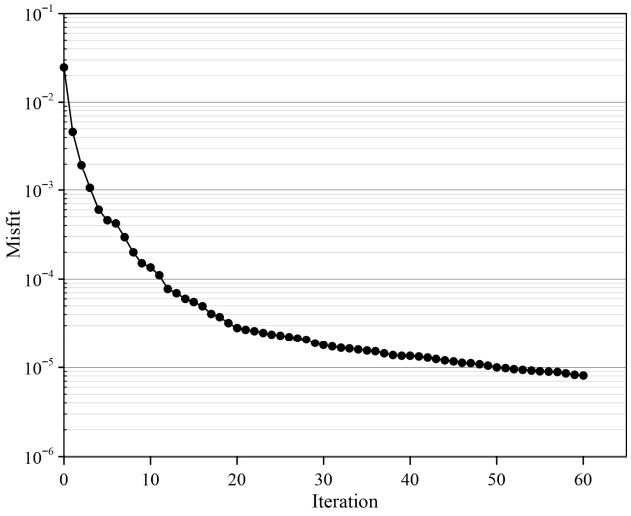


Figure 15. Convergence curves of 3D inversion misfits for the hydrocarbon reservoir model.

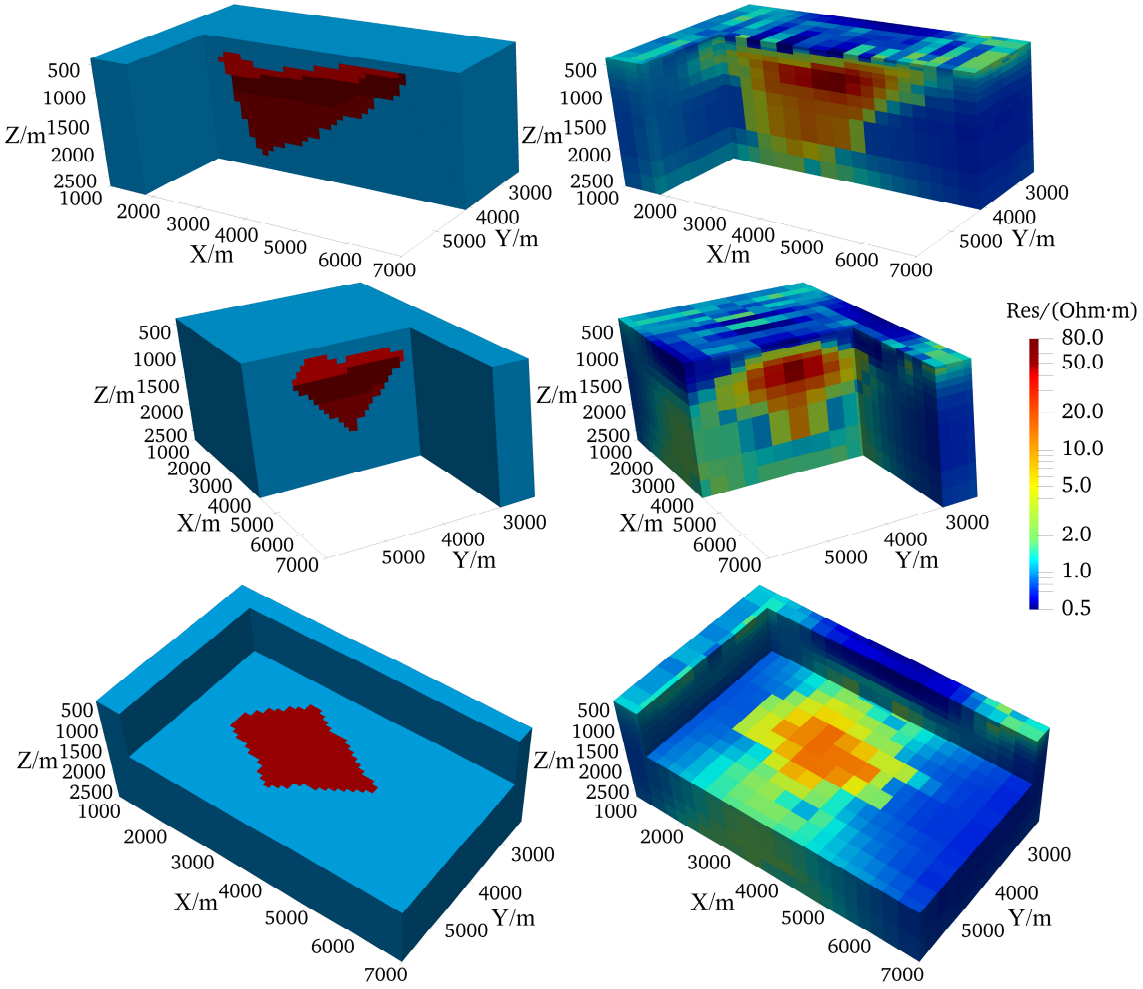


Figure 16. Three-dimensional views of the true resistivity model and the recovered resistivity model from the 3D inversion for the hydrocarbon reservoir model.

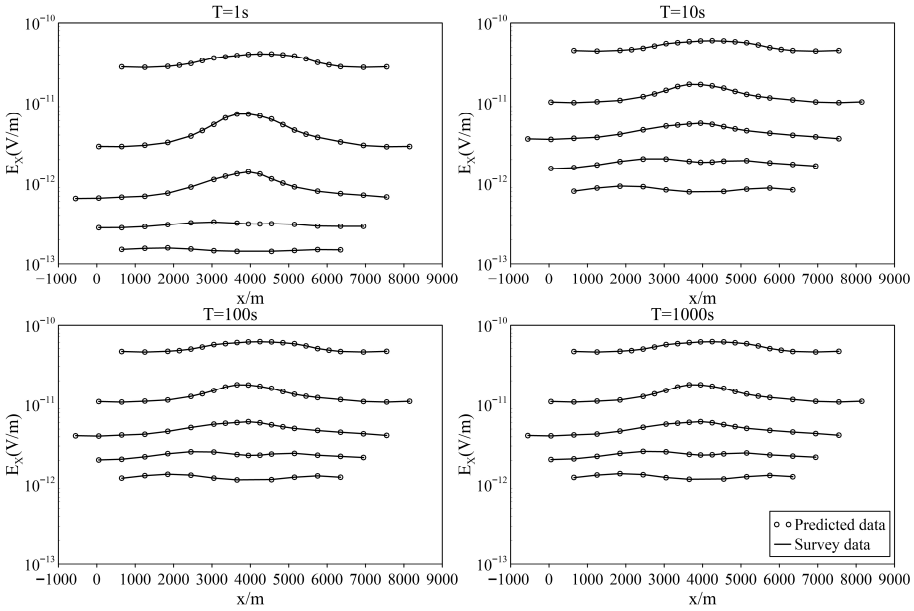


Figure 17. Data fitting results for the survey line y = 1000 m. The five curves in each panel represent data at offsets of 750 m, 1500 m, 2250 m, 3000 m, and 3750 m from top to bottom.

4.2. Salt Dome Model

To verify the detection capability of the marine TDEM method for complex resistive anomalies, a three-dimensional salt dome model was constructed under complex geological conditions. The model was modified from a shallow-water marine seismic velocity model and converted into a resistivity distribution model using the electrical parameter transformation relationship proposed by Gallardo and Mohamed [32] The anomalous body was assigned non-uniform resistivity values to more realistically represent the complexity of electrical structures in actual geological environments.

As shown in Figure 18, the background medium resistivity ranges from 1 to 5 Ω·m, whereas the salt dome anomaly exhibits significantly higher resistivity, with values ranging from 200 to 400 Ω·m. The spatial extent of the anomalous body is defined as 2370 < x < 5730 m, 3080 < y < 6520 m, and 600 < z < 3800 m. The model is discretized using grid spacings of 80 m × 80 m × 160 m in the x, y, and z directions, respectively.

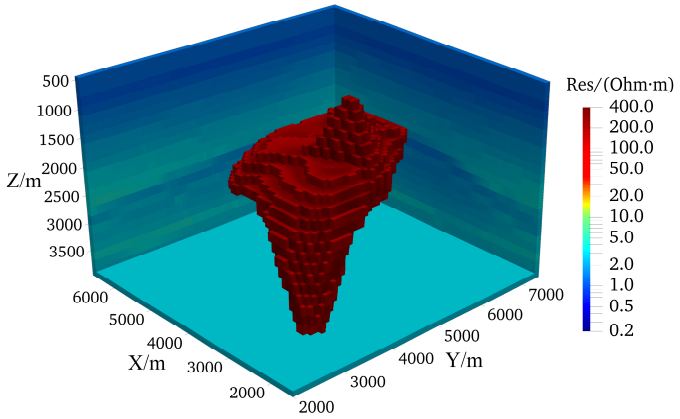


Figure 18. 3D mesh discretization of the salt dome model under complex geological conditions.

Survey lines are uniformly distributed along y = [2400:300:5700] m. On each survey line, transmitters are placed at 600 m intervals within the range x = [−3900:600:9900] m, while receivers are deployed at 300 m intervals within x = [1500:300:6000] m. Frequency domain responses are calculated at frequencies of $10^{(-6:0.2:6)}$ Hz. Step-on responses are then

obtained through frequency to time transformation, and a time window of $10^{(-0.5:0.1:3.5)}$ s is selected to capture stable TDEM response characteristics.

The inversion process stabilized after 60 iterations. As shown in Figure 19, the misfit reduction curve gradually levels off, indicating a relatively fast convergence rate of the algorithm. The 3D slice results (Figure 20) demonstrate that, despite some numerical deviations in resistivity relative to the original model, the inversion accurately identifies the spatial extent of the anomalous body and effectively reconstructs its fundamental morphological characteristics, even under complex background resistivity conditions. These results (Figure 21) indicate that the proposed inversion strategy is highly effective and practical for highly complex geological models.

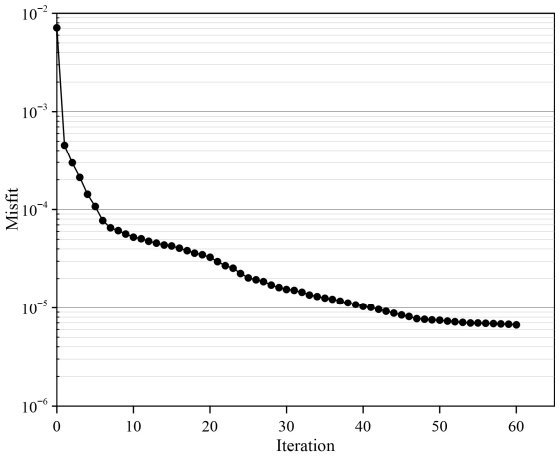


Figure 19. Convergence plot of 3D inversions misfits for the salt dome model.

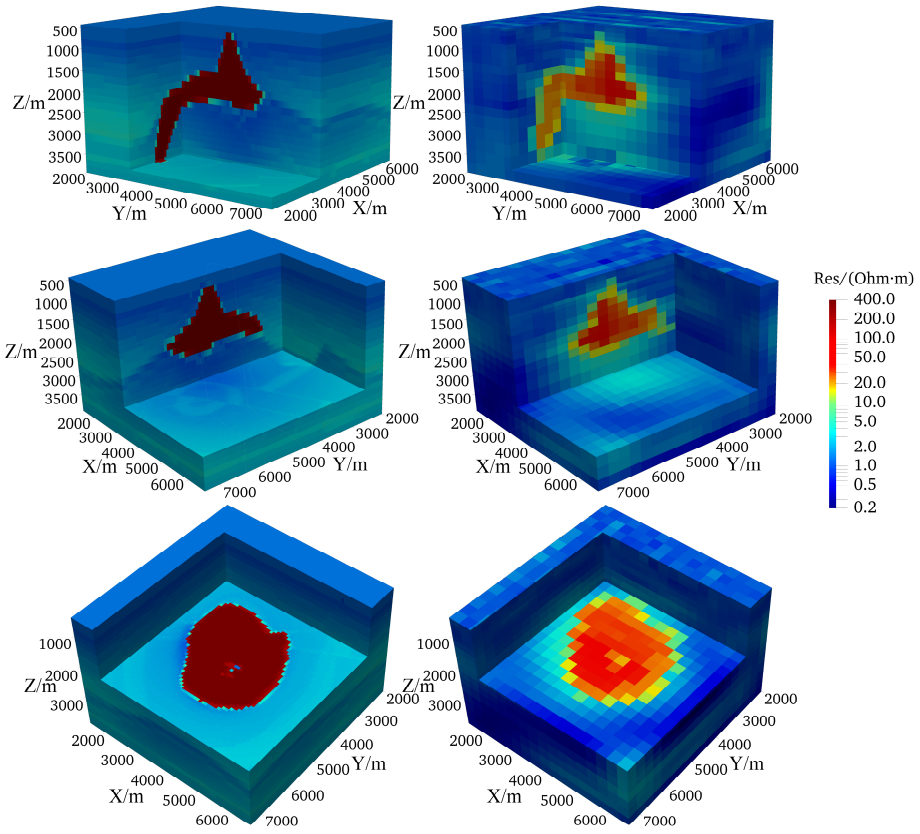


Figure 20. 3D views of the true resistivity model and the recovered resistivity model from the 3D inversion for the salt dome model.

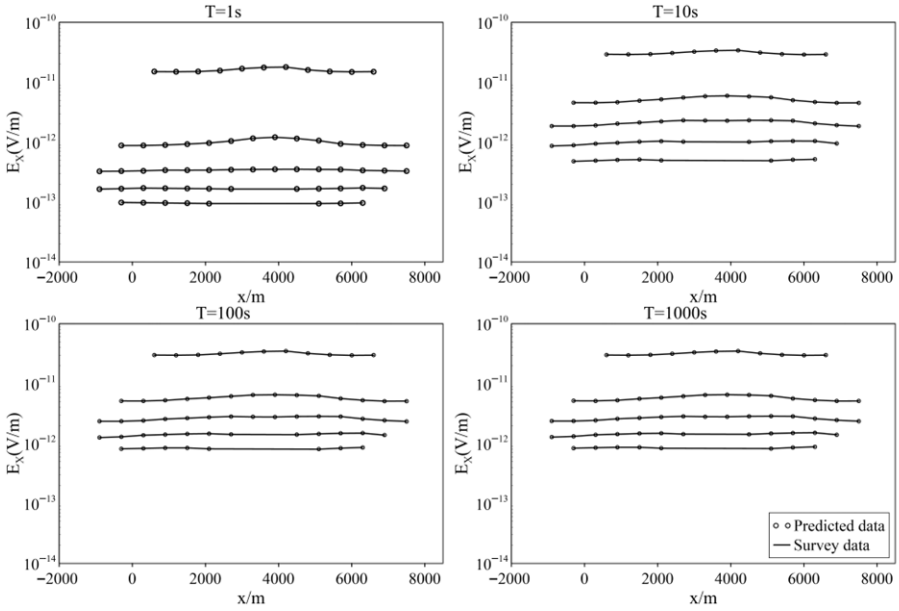


Figure 21. Comparison between observed data and forward responses from the inverted model for the hydrocarbon reservoir.

5. Conclusions

This study proposes an efficient inversion approach based on the moving footprint technique and examines the main factors that control the footprint domain. The main conclusions are summarized as follows:

By introducing the footprint technique, a linear relationship between the footprint domain size and the transmitter–receiver offset is established, thereby defining the effective sensitivity range. This approach effectively alleviates the computational bottleneck caused by the 3D sensitivity matrix's excessive size. The analysis indicates that the footprint domain is primarily controlled by time, seawater depth, subsurface resistivity, and offset distance, whereas background resistivity has a relatively minor influence. From a survey design perspective, placing receivers on the seafloor effectively mitigates interference from the conductive seawater layer on sensitivity distribution, a conclusion confirmed by numerical experiments.

A weighting matrix is constructed to sparsify the dense sensitivity matrix through weighted processing. This transformation significantly reduces memory consumption and substantially decreases both computational time and memory requirements per iteration—particularly at small offsets—while maintaining inversion accuracy comparable to that of the full domain approach.

The reliability and stability of the developed algorithm are validated using two complex 3D synthetic models. The inversion results show good agreement with the true models, accurately reproduce the observed data, and exhibit high computational efficiency and low memory demand, thereby demonstrating the feasibility and practical applicability of the proposed method for marine TDEM exploration.

Author Contributions: Conceptualization, X.W. and S.L.; methodology, X.W.; software, S.L., Z.H. and Q.S.; validation, S.L., Z.H. and Q.S.; writing—original draft preparation, X.W.; writing—review and editing, S.L., Z.H. and Q.S.; project administration, X.W.; funding acquisition, X.W. All authors have read and agreed to the published version of the manuscript.

Funding: This research was funded by Deep Earth Probe and Mineral Resources Exploration—National Science and Technology Major Project (2025ZD1008504, 2024ZD1002204) and the National Natural Science Foundation of China under Grants 42274185, 42130811 and 41964006.

Data Availability Statement: All data generated and analyzed during this study are included in the article.

Conflicts of Interest: The authors declare no conflicts of interest.

References

1. Eidesmo, T.; Ellingsrud, S.; MacGregor, L.M.; Constable, S.; Sinha, M.C.; Johansen, S.E.; Westerdahl, H. Sea bed logging (SBL), a new method for remote and direct identification of hydrocarbon filled layers in deepwater areas. *First Break* **2002**, *20*, 144–152.
2. Ellingsrud, S.; Eidesmo, T.; Johansen, S.; Sinha, M.C.; MacGregor, L.M.; Constable, S. Remote sensing of hydrocarbon layers by seabed logging (SBL): Results from a cruise offshore Angola. *Lead. Edge* **2002**, *21*, 972–982. [CrossRef]
3. Constable, S. Ten years of marine CSEM for hydrocarbon exploration. *Geophysics* **2010**, *75*, 75A67–75A81. [CrossRef]
4. Shen, J.; Wang, X.; Wei, S.S.; Li, M. Methods of Air Wave Approximation and Decomposition for Marine Controlled Source Electromagnetic Measurements in Shallower Water Domain. *J. Jilin Univ. (Earth Sci. Ed.)* **2015**, *45*, 282–292.
5. Weiss, C.J. The fallacy of the "shallow-water problem" in marine CSEM exploration. *Geophysics* **2007**, *72*, A93–A97. [CrossRef]
6. Barsukov, P.O.; Fainberg, E.B. Transient marine electromagnetics in shallow water: A sensitivity and resolution study of the vertical electric field at short ranges. *Geophysics* **2014**, *79*, E39–E49. [CrossRef]
7. Ziolkowski, A.; Hall, G.; Wright, D.; Carson, R.; Peppe, O.; Tooth, D.; Chorley, P. Shallow marine test of MTEM method. In *Proceedings of the 2006 SEG Annual Meeting, New Orleans, LA, USA, 1–6 October 2006*; Society of Exploration Geophysicists: New Orleans, LA, USA, 2006; pp. 729–734.
8. Schwalenberg, K.; Rippe, D.; Koch, S.; Scholl, C. Marine-controlled source electromagnetic study of methane seeps and gas hydrates at Opouawe Bank, Hikurangi Margin, New Zealand. *J. Geophys. Res. Solid Earth* **2017**, *122*, 3334–3350. [CrossRef]
9. Lippert, K.; Tezkan, B.; Boekmann, J.; Haroon, A. First land application of the differential electrical dipole method together with transient electromagnetics. 24th European Meeting of Environmental and Engineering Geophysics. *Eur. Assoc. Geosci. Eng.* **2018**, *2018*, 1–5.
10. Haroon, A.; Micallef, A.; Jegen, M.; Schwalenberg, K.; Karstens, J.; Berndt, C.; Chidichimo, F. Electrical resistivity anomalies offshore a carbonate coastline: Evidence for freshened groundwater? *Geophys. Res. Lett.* **2021**, *48*, e2020GL091909. [CrossRef]
11. Holten, T.; Flekkøy, E.G.; Singer, B.; Blixt, E.M.; Hanssen, A.; Måløy, K.J. Vertical source, vertical receiver, electromagnetic technique for offshore hydrocarbon exploration. *First Break* **2009**, *27*, 89–93. [CrossRef]
12. Um, E.S.; Alumbaugh, D.L.; Harris, J.M.; Chen, J. Numerical modeling analysis of short-offset electric-field measurements with a vertical electric dipole source in complex offshore environments. *Geophysics* **2012**, *77*, E329–E341. [CrossRef]
13. Singer, B.S.; Atramonova, S. Vertical electric source in transient marine CSEM: Effect of 3D inhomogeneities on the late time response. *Geophysics* **2013**, *78*, E173–E188. [CrossRef]
14. Barsukov, P.O.; Fainberg, E.B. On the sensitivity of transient electromagnetic methods to resistive targets. *Geophys. Prospect.* **2017**, *65*, 263–275.
15. Helwig, S.L.; Jang, H.; Kim, H.J. Investigation of the resolution of ground and airborne TEM methods for resistive targets. *J. Appl. Geophys.* **2019**, *164*, 155–166.
16. Zhou, J.; Li, X.; Xue, G.; Wu, X. A review of transient electromagnetic methods for mineral exploration: Advances and challenges. *Ore Geol. Rev.* **2023**, *152*, 105234.
17. Ziolkowski, A.; Hobbs, B.A.; Wright, D. Multitransient electromagnetic demonstration survey in France. *Geophysics* **2007**, *72*, F197–F209. [CrossRef]
18. Avdeeva, A.; Moorkamp, M. The importance of shallow data in controlled-source electromagnetic (CSEM) data interpretation. *Geophys. Prospect.* **2007**, *55*, 847–857.
19. Moghadas, D.; Engels, M.; Schwalenberg, K. 1D joint multi-offset inversion of time domain marine controlled source electromagnetic data. *Geophys. Prospect.* **2015**, *63*, 1334–1354. [CrossRef]
20. Lippert, T.; Bandelin, J.; Schlederer, F.; Drewes, J.E.; Koch, K. Effects of ultrasonic reactor design on sewage sludge disintegration. *Ultrason. Sonochemistry* **2020**, *68*, 105223. [CrossRef]
21. Moghadas, D.; Behroozmand, A.A.; Christiansen, A.V. Impact of inversion strategies on 1D inversion of time domain marine electromagnetic data. *J. Appl. Geophys.* **2015**, *122*, 163–174.
22. Cai, J.; Tezkan, B.; Li, Y. Effects of the sea floor topography on the 1D inversion of time domain marine controlled source electromagnetic data. *Geophys. Prospect.* **2018**, *66*, 1602–1624. [CrossRef]
23. Frafjord, Ø.; Key, K.; Helwig, S.L.; El Kaffas, A.M.; Holten, T.; Eide, K. Time Domain 2D CSEM Inversion with Induced Polarization. In Proceedings of the 77th EAGE Conference and Exhibition 2015, Madrid, Spain, 1–4 June 2015; Volume 2015, pp. 1–5.
24. Li, W.; Li, X.; Lu, X. Two-dimensional inversion of multi-channel transient electromagnetic data using a cosine transform and MARE2DEM. *Geophysics* **2019**, *84*, E233–E245.

25. Holten, T.; Singer, B.S.; Bratteli, E. Three-dimensional inversion of transient marine electromagnetic data using a conjugate-gradient algorithm. *Geophys. J. Int.* **2014**, *199*, 805–818.
26. Huang, X.; Yan, L.J.; Xie, X.B. 3D AEM forward modeling based on the poly-grid spectral-element method with average weighted conductivity. *Geophys. Prospect. Pet.* **2024**, *63*, 1259–1273.
27. Zhan, W.C.; Chen, Y.J.; Liu, Q.Q.; Li, J.; Sacchi, M.D.; Zhuang, M.; Liu, Q.H. Simultaneous prediction of petrophysical properties and formation layered thickness from acoustic logging data using a modular cascading residual neural network (MCARNN) with physical constraints. *J. Appl. Geophys.* **2024**, *224*, 105362. [CrossRef]
28. Castillo-Reyes, O.; de la Puente, J.; Cela, J.M. PETGEM: A parallel code for 3D CSEM forward modeling using edge finite elements. *Comput. Geosci.* **2018**, *119*, 123–136. [CrossRef]
29. Castillo-Reyes, O.; De la Puente, J.; García-Castillo, L.E.; Cela, J.M. Parallel 3-D marine controlled-source electromagnetic modelling using high-order tetrahedral Nédélec elements. *Geophys. J. Int.* **2019**, *219*, 39–65. [CrossRef]
30. Cox, L.H.; Zhdanov, M.S. Large-scale 3D inversion of HEM data using a moving footprint.SEG Technical Program Expanded Abstracts. *Soc. Explor. Geophys.* **2007**, *26*, 467–471.
31. Cox, L.H.; Wilson, G.A.; Zhdanov, M.S. 3D inversion of airborne electromagnetic data using a moving footprint. *Explor. Geophys.* **2012**, *43*, 178–187. [CrossRef]
32. Gribenko, A.; Green, A.M.; Cuma, M.; Zhdanov, M.S. Efficient 3D inversion of MT data using integral equations method and the receiver footprint approach. SEG Technical Program Expanded Abstracts. *Soc. Explor. Geophys.* **2010**, *29*, 644–649.
33. Liu, Y.; Yin, C.; Ren, X. A footprint-guided airborne electromagnetic inversion method. *Geophysics* **2019**, *84*, E167–E178.
34. Qi, Y.; Ju, Y.; Tan, J.; Bowen, L.; Cai, C.; Yu, K.; Zhang, W. Organic matter provenance and depositional environment of marine-to-continental mudstones and coals in eastern ordos basin, china—Evidence from molecular geochemistry and petrology. *Int. J. Coal Geol.* **2020**, *217*, 103345. [CrossRef]
35. Zhang, P.; Yin, C.; Liu, Y. 3-D inversion of frequency domain airborne electromagnetic data with a footprint-based local mesh method. *Geophysics* **2021**, *86*, E337–E349. [CrossRef]
36. Key, K. Is the fast Hankel transform faster than quadrature? *Geophysics* **2012**, *77*, F21–F30. [CrossRef]
37. Zhdanov, M.S.; Endo, M.; Cox, L.H.; Čuma, M.; Linfoot, J.; Anderson, C.; Black, N.; Gribenko, A.V. Three-dimensional inversion of towed streamer electromagnetic data. *Geophys. Prospect.* **2014**, *62*, 552–572. [CrossRef]
38. Tølbøll, R.J.; Christensen, N.B. Sensitivity functions of frequency domain magnetic dipole-dipole systems. *Geophysics* **2007**, *72*, F45–F56. [CrossRef]
39. Yin, C.C.; Huang, X.; Liu, Y.H.; Cai, J. Footprint for frequency domain airborne electromagnetic systems. *Geophysics* **2014**, *79*, E243–E254. [CrossRef]

Disclaimer/Publisher's Note: The statements, opinions and data contained in all publications are solely those of the individual author(s) and contributor(s) and not of MDPI and/or the editor(s). MDPI and/or the editor(s) disclaim responsibility for any injury to people or property resulting from any ideas, methods, instructions or products referred to in the content.